

# Chapter 23

## Atomistic Tight-Binding Study of Core/Shell Nanocrystals



Worasak Sukkabot

**Abstract** Progressive technologies in the synthetic chemistry of semiconductor nanostructures have made it possible to access high quality semiconductor nanostructures with precise size, shape and composition. Colloidal core/shell nanocrystals are composed of a core made from one material terminated by a shell of another material. Because of the improved photoluminescence quantum yields, high photostability and size-tunable emission properties, core/shell nanocrystals are tremendously attractive for the active applications. The purpose of this chapter is to present the atomistic tight-binding theory to study the electronic structures and optical properties of core/shell nanocrystals with the purpose to evidently understand the significance of core and growth shell. Owing to the heterostructure of core/shell nanocrystal, the valence force field method is utilized to optimize the structural geometry. To analyze the electronic structures and optical properties of the core/shell nanocrystals with the corresponding structural parameters, some of the calculations are demonstrated. Finally, all-inclusive information based on atomistic tight-binding theory successfully conveys the natural behaviors of core/shell nanocrystals and carries a guideline for the design of their electronic and optical properties before applying to the novel electronic nanodevices.

### 23.1 Introduction

Advanced technologies in the synthetic chemistry of semiconductor nanostructures have made it possible to access high quality semiconductor nanostructures with controlled size, shape and composition. Nanostructures containing more than one material can easily be synthesized nowadays. Core/shell nanocrystal is one of the nanostructures composed of a core made from one material terminated by a shell of another material. Therefore, the structural, electronic, magnetic and optical properties of the core/shell nanocrystals can be manipulated not only by the core but also by the

---

W. Sukkabot (✉)

Faculty of Science, Department of Physics, Ubon Ratchathani University, 85 Sathollmark Rd., Warinchamrab, Ubon Ratchathani 34190, Thailand

growth shell. The advantages in the improved photoluminescence quantum yields, high photostability and size-tunable emission properties make core/shell nanocrystals extremely gorgeous for widespread applications such as light-emitting diodes [1, 2], solar cells [3–6], lasers [7], biological imaging [8–11] and quantum information [12–16]. Before the authentic manufacture, the theoretical description of semiconductor nanostructures is of crucial importance because of its allowance to analyze and predict the fundamental physics. Here, it is the aim of this chapter to provide the reader with a comprehensive overview of the band structure calculations of core/shell semiconductor nanocrystals. We take a special emphasis on the empirical tight-binding description and valence force field method in order to deliver some of their calculations.

To study the electronic and optical properties of semiconductor nanostructures, the band structures are required to be understood. At the moment, there are several theoretical calculations of the band structures such as k.p method [17–25], tight-binding model [26–35], pseudopotential model [36–42] and density functional theory [43–46]. Each method has their own technique to calculate the band structures of semiconductors. Conventionally, the nanostructures are investigated by k.p method in the framework of the envelope function approximation (EFA) [47–49]. This approach mainly lacks the atomic detail. Because of a reasonable compromise between the computational resource and the reliability of the results, k.p method still remains to be implemented. Advanced technologies of the synthesis make it possible to fabricate the high quality semiconductor nanostructures with complexity where k.p method hardly deals with. Hence, the envelope function concept is replaced by density functional theory. However, the realistic nanostructures contain an amount of atoms where density functional theory encounters the dimensionality of the problem. Presently, advanced density functional calculations under large parallel supercomputers can be applied to study the structures with several thousand atoms. With the aim to mainly preserve both of the computational efficiency and atomistic detail, the empirical methods are the suitable candidates for modelling the nanostructure devices. Two empirical methods are proposed for atomistic nanostructure description, namely the empirical tight-binding approach (ETB) and the empirical pseudopotential technique (EPM). ETB method yields the simple and appealing calculations using bonding properties in the framework of orbital occupations and orbital overlap. ETB approach overcomes k.p method due to the consideration of atomic details, while the computationally consuming time of ETB model is comparable to that of k.p method. Another strength is that the scalability of ETB approach can be investigated up to the level of the density function theory. However, the disadvantage of ETB method is the large number of parameters involved to accurately reproduce the band structures. The EPM represents the precise band structures with a few parameters, thus reducing the restrictions of ETB approach. For the demonstration of the accurate band structures, EPM method must be based on the wave function expansion produced from the large number of plane waves. Within the tight-binding model, the wave function is spanned with a small basis set depending on the included orbitals, number of atoms and neighboring interactions. Hence, ETB model is computationally less expensive than EPM model. According to the argument, ETB model is a good applicant for the

study of relatively big and complicated systems in which both of the computational efficiency and atomistic description are preserved.

The main objective of this chapter is to give the comprehensive description of computational tool for the nanostructure devices. The computational tool consists of the valence force field method and empirical tight-binding theory. Valence force field method is implemented to optimize the atomic positions. After obtaining the relaxed structures, the electronic and optical properties are determined in the framework of empirical tight-binding model. This chapter is also to deliver primarily our own work and a rudimentary attempt is made to cover the wide literature on this subject. The chapter is organized as follow. Section 23.2 provides the description of the valence force method. In Sect. 23.3, the principle of the empirical tight-binding method is applied to the bulk semiconductors with different tight-binding hybridizations. The implementation of the  $sp^3s^*$  empirical tight-binding method into the core/shell semiconductor nanocrystals is demonstrated in Sect. 23.4. Finally, the summary is provided in Sect. 23.5.

## 23.2 Valence Force Field

Due to the lattice mismatch between core and shell material, the atomic positions inside and around core/shell nanocrystal are distorted. To optimize the structural geometry, there are two major methods, continuum elasticity [50–53] and atomistic elasticity approach [50, 54–61]. In this work, the valence force field method (VFF), one of the atomistic elasticity approaches, is implemented to relax the atomic positions of the core/shell nanocrystal. The advantage of the valence force field is that it includes atomic scale information such as inter-atomic potential and correct point group symmetry. For the demonstration, the atoms in core/shell nanocrystal are considered as point particles and the bonds are termed as springs. Therefore, the equation of the spring deformation is theoretically used to explain the behavior of the stretching and bending bonds. The objective of this approach is to minimize the energy associated with a given atomic structure. The total energy of this model is the summation of the energy of the stretching and bending of the bonds. The expression of total energy is described in term of the fitting parameters which explain the behaviors of different kinds of the atoms in core/shell nanocrystal. After relaxing the atomic positions, the strain distribution and strain tensors are attained.

### 23.2.1 Valence Force Field Method (VFF)

In the realistic structures, core and shell are chemically synthesized from different materials with their own lattice constants, leading to the lattice-mismatch-induced strain in such structure. For example, the mismatch for InAs core passivated by GaAs shell is 6%, while for InAs core terminated by InP shell it is about 3%. To calculate

the optimized atomic positions of core/shell nanocrystal, strain relaxation has been provided. In this work, the valence force field method is implemented for atomistic optimization. The elastic energy of all atoms is expressed as a function of the atomic positions  $R_i$  as:

$$E = \sum_{ij} V_2(R_i - R_j) + \sum_{ij} V_3(\theta_{ijk})$$

where  $V_2$  is the two-body term called stretching function,  $V_3$  is the three body term of the bond angle called bending function and  $\theta_{ijk}$  is the angle subtended at the atom  $i$  by atoms  $j$  and  $k$ . The actual formula for the total elastic energy is given by:

$$E = \sum_i \sum_{j=1}^4 \frac{3\alpha_{ij}}{16(d_{ij}^0)^2} [(R_j - R_i)^2 - (d_{ij}^0)^2]^2 + \sum_i \sum_{j,k>1}^4 \frac{3\beta_{ijk}}{8d_{ij}^0 d_{ik}^0} [(R_j - R_i) \cdot (R_k - R_i) - \cos \theta d_{ij}^0 d_{ik}^0]^2$$

Here,  $d_{ij}^0$  denotes the bulk equilibrium bond length between the nearest-neighbor atom  $i$  and  $j$  in the corresponding binary compound and  $\theta = \arccos(1/3)$  is the ideal bond angle of zinc-blende structure. The first term is a sum over all atom  $i$  and its nearest neighbours  $j$ . The second term is a sum over all atoms  $i$  and distinct pairs of its nearest neighbours  $j$  and  $k$ . The fitting dependent parameters  $\alpha$  and  $\beta$  are the bond-stretching and bond-bending force constants, respectively. For the bending term at the interface where the species  $j$  and  $k$  are different, the average of the corresponding values of these pure semiconductors is utilized. Table 23.1 lists the parameters  $\alpha$  and  $\beta$  of the the important semiconductors (mainly in III–V and II–VI group) [62].

**Table 23.1** The parameters  $\alpha$  and  $\beta$  of the the important semiconductors (mainly in III–V and II–VI group) [62]

Semiconductor	$\alpha$ (N/m)	$\beta$ (N/m)
InAs	35.04	6.14
InP	38.56	6.75
InSb	28.68	5.02
GaAs	41.70	7.30
GaP	48.18	8.44
GaSb	31.68	5.55
CdS	33.43	3.54
CdSe	29.64	3.14
ZnO	69.67	7.38
ZnS	42.16	4.46

To calculate the relaxed atomic positions of the core/shell nanocrystals, the total elastic energy is minimized with respect to the atomic positions  $R_i$ . Here, the conjugate gradient method (CGDESCENT) [63–65] developed by William W. Hager is implemented. Once the relaxed atomic positions of all atoms are known, the strain distribution is realized through the strain tensors. The cation site is formed a tetrahedron bonding to its four nearest neighboring anions. The strain tensors  $\varepsilon$  are calculated from the correlation between the distorted and ideal tetrahedron edges. The distorted tetrahedron edges,  $R_{12}$ ,  $R_{23}$  and  $R_{34}$ , are connected to the ideal tetrahedron edges,  $R_{12}^0$ ,  $R_{23}^0$  and  $R_{34}^0$ , from this relation: [50]

$$\begin{bmatrix} R_{12,x} & R_{23,x} & R_{34,x} \\ R_{12,y} & R_{23,y} & R_{34,y} \\ R_{12,z} & R_{23,z} & R_{34,z} \end{bmatrix} = \begin{bmatrix} 1 + \varepsilon_{xx} & \varepsilon_{yx} & \varepsilon_{zx} \\ \varepsilon_{xy} & 1 + \varepsilon_{yy} & \varepsilon_{zy} \\ \varepsilon_{xz} & \varepsilon_{yz} & 1 + \varepsilon_{zz} \end{bmatrix} \begin{bmatrix} R_{12,x}^0 & R_{23,x}^0 & R_{34,x}^0 \\ R_{12,y}^0 & R_{23,y}^0 & R_{34,y}^0 \\ R_{12,z}^0 & R_{23,z}^0 & R_{34,z}^0 \end{bmatrix}$$

The strain tensors are then calculated by the matrix inversion as:

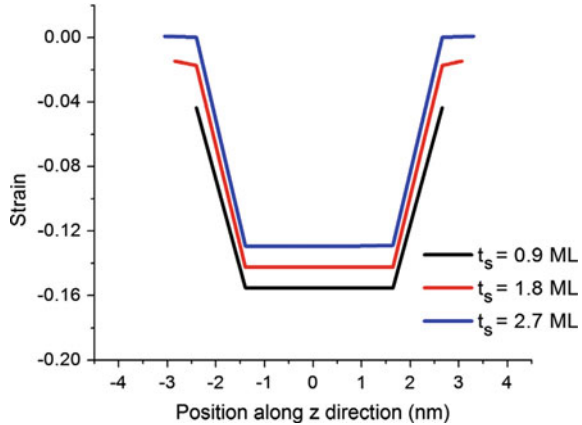
$$\begin{bmatrix} \varepsilon_{xx} & \varepsilon_{yx} & \varepsilon_{zx} \\ \varepsilon_{xy} & \varepsilon_{yy} & \varepsilon_{zy} \\ \varepsilon_{xz} & \varepsilon_{yz} & \varepsilon_{zz} \end{bmatrix} = \begin{bmatrix} R_{12,x} & R_{23,x} & R_{34,x} \\ R_{12,y} & R_{23,y} & R_{34,y} \\ R_{12,z} & R_{23,z} & R_{34,z} \end{bmatrix} \begin{bmatrix} R_{12,x}^0 & R_{23,x}^0 & R_{34,x}^0 \\ R_{12,y}^0 & R_{23,y}^0 & R_{34,y}^0 \\ R_{12,z}^0 & R_{23,z}^0 & R_{34,z}^0 \end{bmatrix}^{-1} - I$$

where  $I$  is the  $3 \times 3$  identity matrix.

### 23.2.2 Examples of the Calculations

Here, the examples in the implementation of the valence force field method on the core/shell nanostructures are demonstrated. The nanocrystals and nanorods of CdSe and CdS are excellent candidates for the novel optical and electronic applications. Luo and Wang [66] optimized the atomic positions of CdSe/CdS core/shell nanorod. The spherical CdSe core with a diameter of 3.44 nm at the right-hand side of the nanorod was surrounded by CdS rod with diameter of 4.30 nm and the length of 15.48 nm. Due to the lattice mismatch between core and shell material, the compressive strain was found in CdSe core, while the tensile strain was observed nearby CdSe core and in CdSe shell. In CdS shell far away from CdSe core, there was no strain influence. CdSe/ZnSe core/shell nanocrystal is one of the outstanding candidates to provide the high luminescence quantum yields. Due to the lattice mismatch between core and shell, the induced strain in CdSe/ZnSe core/shell nanocrystals with experimentally synthesized sizes was studied by Sukkabet [67]. The ZnSe shell thicknesses ( $t_s$ ) of 0.9, 1.8 and 2.7 monolayer (ML) were consecutively passivated on CdSe core with diameter of 3.6 nm. Figure 23.1 displayed the hydrostatic strains ( $\varepsilon_{xx} + \varepsilon_{yy} + \varepsilon_{zz}$ ) in the  $z$  direction through the middle of the core/shell nanocrystal under different shell thicknesses. The hydrostatic strains were mainly sensitive with the growth shell

**Fig. 23.1** Hydrostatic strains ( $e_{xx} + e_{zz} + e_{zz}$ ) of CdSe/ZnSe core/shell nanocrystals as a function of ZnSe shell thicknesses (ML) [67]



thickness. The compressive strains were probed in the core region within all shell dimensions, whereas there was no tensile strain in core and shell.

### 23.3 Empirical Tight-Binding Method

The empirical tight-binding theory was initially developed by Slater and Koster [68]. Within the empirical tight-binding theory, Hamiltonian matrix elements are elucidated by fitting parameters. These parameterizations can reproduce the reference quantities such as the band structure, effective mass or band gap derived by first-principles calculations or extracted from experimental data. The empirical tight-binding method is often used to study electronic and optical properties of nanostructure devices. Before developing the nanostructure description, it is essential to describe bulk semiconductors and matrix element parameters. Here,  $sp^3s^*$  empirical tight-binding method is used to determine the bulk semiconductors. The historical parameterization is described with the increasing including orbitals starting from the minimal  $sp^3$  basis.

#### 23.3.1 The Bulk Hamiltonian

In the term of the bulk semiconductor, the one-electron wavefunctions  $|\ln k\rangle$  can be written as Bloch functions due to the symmetry of the system as given by:

$$|\psi_{n,k}\rangle = \sum_{\alpha,\beta} C_{\alpha\beta}(n,k) \left\{ \sum_R e^{ik \cdot R\beta} |\alpha, R\beta\rangle \right\}$$

For the convenience,  $R_\beta = R + d_\beta$  where  $R$  is the lattice vector and  $d_\beta$  is the atomic position.  $\beta$  and  $\alpha$  refer to the index of the atom and to the atomic orbital index, respectively.  $C_{\alpha\beta}(n, k)$  are the coefficients of the linear combination which depend on the band index  $n$  and the  $k$  vector in Brillouin zone. The expansion of the one-electron wavefunction utilizes a complete set of basis functions. In the tight-binding method, the basis used in the linear combination contains the atomic states of the outermost occupied valence electron states. The coefficients  $C_{\alpha\beta}(n, k)$  of the linear expansion are carried out by solving the well-known Schrodinger equation:

$$H|\psi_{n,k}\rangle = E_n(k)|\psi_{n,k}\rangle$$

where  $E_n(k)$  symbolizes the energy band dispersion. To obtain the energies and one-electron wavefunctions, quantum matrix is implemented with assistance of the hopping matrix elements. Then, the one-electron tight-binding Hamiltonian is written in term of the localized basis as:

$$H = \sum_{\alpha, R_\beta} |\alpha, R_\beta\rangle \varepsilon_{\alpha, \beta} \langle \alpha, R_\beta| + \sum_{\alpha, \alpha', R_{\beta'} \neq R_\beta} |\alpha', R_{\beta'}\rangle t_{\alpha\alpha'} \langle \alpha, R_\beta|$$

The first term stands for  $R_{\alpha'} = R_\alpha$  and  $\alpha' = \alpha$ , namely the on-site matrix elements:

$$\varepsilon_{\alpha, \beta} = \langle \alpha, R_\beta | H | \alpha, R_\beta \rangle$$

The second term stands for  $R_{\beta'} \neq R_\beta$ , called the off-site matrix elements:

$$t_{\alpha'\alpha}(R_{\beta'} - R_\beta) = \langle \alpha', R_{\beta'} | H | \alpha, R_\beta \rangle$$

For the demonstration of the bulk band calculations, the tight-binding method with the combination of minimal  $sp^3$  basis (one  $s$  orbital and three  $p$  orbitals) plus the excited  $s$  state with  $s$ -like symmetry ( $s^*$ ), called  $sp^3s^*$  empirical tight-binding approach. This empirical tight-binding model has been widely implemented for various nanostructures. In this chapter,  $sp^3s^*$  empirical tight-binding method with the nearest-neighboring interaction is applied to the zinc-blende structures. The independent tight-binding parameterizations consisting of on-site energies ( $\varepsilon_{s,a(c)}$ ,  $\varepsilon_{p,a(c)}$  and  $\varepsilon_{s^*,a(c)}$ ) and off-site matrix elements ( $V$ ) are demonstrated as:

$$V_{ss} = 4t_{ss}(R_a - R_c)$$

$$V_{xx} = 4t_{p_x p_x}(R_a - R_c)$$

$$V_{xy} = 4t_{p_x p_y}(R_a - R_c)$$

$$V_{s p_x} = 4t_{s p_x}(R_a - R_c)$$

$$V_{p_x s} = 4t_{p_x s}(R_a - R_c)$$

$$V_{s^* p_x} = 4t_{s^* p_x}(R_a - R_c)$$

$$V_{p_x s^*} = 4t_{p_x s^*}(R_a - R_c)$$

Here, a and c present the anion and cation atoms. The interaction between s \* orbitals is neglected. Finally, the 10 × 10 Hamiltonian matrix is given by:

$$\begin{bmatrix} \epsilon_{s,a} & 0 & 0 & 0 & 0 & V_{ss}g_0 & V_{sp}g_1 & V_{sp}g_2 & V_{sp}g_3 & 0 \\ 0 & \epsilon_{p,a} & 0 & 0 & 0 & -V_{ps}g_1 & V_{xx}g_0 & V_{xy}g_3 & V_{xy}g_2 & -V_{ps^*}g_1 \\ 0 & 0 & \epsilon_{p,a} & 0 & 0 & -V_{ps}g_2 & V_{xy}g_3 & V_{xx}g_0 & V_{xy}g_1 & -V_{ps^*}g_2 \\ 0 & 0 & 0 & \epsilon_{p,a} & 0 & -V_{ps}g_3 & V_{xy}g_2 & V_{xy}g_1 & V_{xx}g_0 & -V_{ps^*}g_3 \\ 0 & 0 & 0 & 0 & \epsilon_{s^*,a} & 0 & V_{s^*p}g_1 & V_{s^*p}g_2 & V_{s^*p}g_3 & 0 \\ V_{ss}g_0^* & -V_{ps}g_1^* & -V_{ps}g_2^* & -V_{ps}g_3^* & 0 & \epsilon_{s,c} & 0 & 0 & 0 & 0 \\ V_{sp}g_1^* & V_{xx}g_0^* & V_{xy}g_3^* & V_{xy}g_2^* & V_{s^*p}g_1^* & 0 & \epsilon_{p,c} & 0 & 0 & 0 \\ V_{sp}g_2^* & V_{xy}g_3^* & V_{xx}g_0^* & V_{xy}g_1^* & V_{s^*p}g_2^* & 0 & 0 & \epsilon_{p,c} & 0 & 0 \\ V_{sp}g_3^* & V_{xy}g_2^* & V_{xy}g_1^* & V_{xx}g_0^* & V_{s^*p}g_3^* & 0 & 0 & 0 & \epsilon_{p,c} & 0 \\ 0 & V_{ps^*}g_1^* & V_{ps^*}g_2^* & V_{ps^*}g_3^* & 0 & 0 & 0 & 0 & 0 & \epsilon_{s^*,c} \end{bmatrix}$$

In this matrix, the  $g_i$  coefficients depend on the wave vectors  $k$ . These values are defined as:

$$g_0(k) = \frac{1}{4} [e^{ik \cdot \tau_1} + e^{ik \cdot \tau_2} + e^{ik \cdot \tau_3} + e^{ik \cdot \tau_4}]$$

$$g_1(k) = \frac{1}{4} [e^{ik \cdot \tau_1} - e^{ik \cdot \tau_2} + e^{ik \cdot \tau_3} - e^{ik \cdot \tau_4}]$$

$$g_2(k) = \frac{1}{4} [e^{ik \cdot \tau_1} - e^{ik \cdot \tau_2} - e^{ik \cdot \tau_3} + e^{ik \cdot \tau_4}]$$

$$g_3(k) = \frac{1}{4} [e^{ik \cdot \tau_1} + e^{ik \cdot \tau_2} - e^{ik \cdot \tau_3} - e^{ik \cdot \tau_4}]$$

where the vectors  $\tau_i$  are the distances between the nearest-neighboring atoms in the zinc-blende structure given by:

$$\tau_1 = \frac{A_0}{4} (\hat{i} + \hat{j} + \hat{k})$$

$$\tau_2 = \frac{A_0}{4} (-\hat{i} - \hat{j} + \hat{k})$$



$$\tau_3 = \frac{A_0}{4} (\hat{i} - \hat{j} - \hat{k})$$

$$\tau_4 = \frac{A_0}{4} (-\hat{i} + \hat{j} - \hat{k})$$

Here,  $A_0$  is lattice constant of the studied zinc-blende semiconductor.

For the realistic situation, the spin-orbit interaction is included in  $sp^3s^*$  empirical tight-binding Hamiltonian as described by Chadi [69]. Considering a spherical symmetric potential, the spin-orbit interaction is defined as:

$$H_{so} = \frac{\hbar}{4m^2c^2} \frac{1}{r} \frac{dV_C(r)}{dr} L \cdot \sigma$$

Here,  $\sigma$  are the Pauli matrices,  $V_C$  is the crystal potential and  $L$  is the angular momentum. Then, the spin-orbit matrix elements with spin components  $s$  ( $s = \uparrow, \downarrow$ ) are given by:

$$\langle \alpha, R_\beta, s | H_{SO} | \alpha', R_{\beta'}, s' \rangle = \langle \alpha, R_\beta | \frac{\hbar}{4m^2c^2} \frac{1}{r} \frac{dV_C(r)}{dr} L | \alpha', R_{\beta'} \rangle \cdot \langle s | \sigma | s' \rangle$$

For the tight-binding approximation, contributions on the same atom are only considered. Then, the non-zero matrix elements of spin-orbit interaction are demonstrated:

$$\langle p_x, R_\beta, \uparrow | H_{SO} | p_y, R_\beta, \uparrow \rangle = -i\lambda_\beta$$

$$\langle p_x, R_\beta, \downarrow | H_{SO} | p_y, R_\beta, \downarrow \rangle = i\lambda_\beta$$

$$\langle p_z, R_\beta, \uparrow | H_{SO} | p_x, R_\beta, \downarrow \rangle = -\lambda_\beta$$

$$\langle p_z, R_\beta, \downarrow | H_{SO} | p_x, R_\beta, \uparrow \rangle = \lambda_\beta$$

$$\langle p_y, R_\beta, \uparrow | H_{SO} | p_z, R_\beta, \downarrow \rangle = -i\lambda_\beta$$

$$\langle p_y, R_\beta, \downarrow | H_{SO} | p_z, R_\beta, \uparrow \rangle = -i\lambda_\beta$$

$\lambda_\beta$  ( $\lambda_a, \lambda_c$ ) are the spin-orbit splittings of the anion and cation of p orbitals. In empirical tight-binding method, these values are the fitting parameters. Finally, the introduction of the spin-orbit interaction into  $sp^3s^*$  empirical tight-binding Hamiltonian of a zinc-blende structure doubles to the  $20 \times 20$  Hamiltonian matrix.

### 23.3.2 Empirical Tight-Binding Parameterization

To obtain the reliable results of the empirical tight-binding method, the parameterization is a main point which depends on the interesting applications. In the band structure analysis, the data such as effective masses and band gaps need to be reproduced with the density functional calculations and experiments. These parameterizations can be implemented to study the structural, electronic and optical properties of nanostructure devices. There are numerous tight-binding parameterizations of semiconductors introduced by several authors. J. C. Slater and G. F. Koster initially studied the linear combination of atomic orbitals (LCAO) or tight binding, approximation with orthogonalized plane-wave methods to calculate the band structures of simple cubic, face-centered cubic, body-centered cubic and diamond structures. Using the  $sp^3$  tight-binding method with the nearest neighboring interaction [70], the valence bands are described in a proper feature in the comparison with the pseudopotential method. However,  $sp^3$  empirical tight-binding method fails to generate the accurate conduction bands. This problem is revised by including more excited energy orbitals or the orders of the neighboring interactions. Niquet et al. [71] proposed the  $sp^3$  tight-binding model with up to third-nearest neighboring interactions to Si band structure. The tight-binding band structure was excellent to fit with the GW model.

The modification of the parameterizations has been reported by Vogl et al. [72] by introducing an additional  $s^*$  orbital with higher energy, called  $sp^3s^*$  empirical tight-binding method. Using this basis, both valence and conduction bands of various IV, III–V and II–VI semiconductors with direct and indirect band gap are accurately reported. The band structure of Si semiconductor plotted along the high symmetry of the Brillouin zone is illustrated in Fig. 23.2. This  $sp^3s^*$  empirical tight-binding model has been successfully applied to semiconductor nanostructures. However, the  $sp^3s^*$  tight-binding model cannot properly fit the X point in the Brillouin zone. Therefore, its applicability to model the nanostructures is limited in the semiconductor nanostructures where the natural properties are described in X point of the Brillouin zone.

**Fig. 23.2** The  $sp^3s^*$  tight-binding band structure of Si semiconductor along the high symmetry of the Brillouin zone

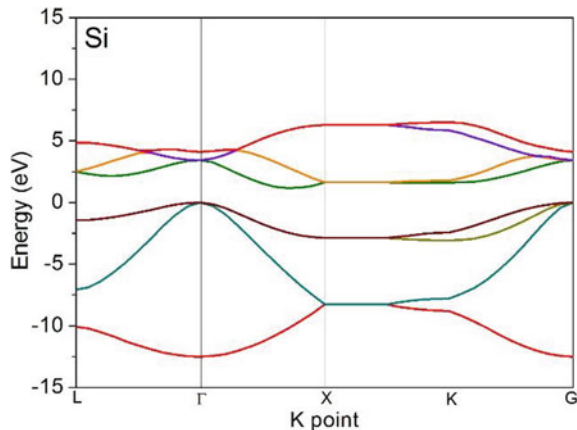


**Table 23.2** Empirical tight-binding models with their references of parameterizations

Semiconductor	$sp^3$ TB	$sp^3s^*$ TB	$sp^3d^5s^*$ TB
<i>IV</i>			
Si	[76–78]	[72, 75]	[73]
Ge	[76–78]	[72]	[73]
SiC	[79]	[72]	[73]
<i>III–V</i>			
GaAs	[85]	[72, 75, 80–84]	[73]
AlAs	[70]	[72, 75, 80–83]	[73]
InAs	[85, 87]	[72, 75, 80, 83, 86]	[73]
GaP	[85]	[72, 75, 83]	[73]
AlP		[72, 75]	[73]
InP	[85]	[72, 75, 80, 83]	[73]
GaSb		[72, 75]	[73]
<i>II–VI</i>			
ZnSe		[72, 75, 84, 88–92]	
CdSe	[93]	[88, 94, 95]	
ZnTe		[72, 75, 88–90]	
CdTe	[98, 99]	[88, 96, 97]	
HgTe	[98, 99]	[88, 96]	
ZnS	[93]	[84, 88, 89]	
CdS	[93, 100]	[88]	
ZnO	[93, 101]		

In order to overcome the restrictions, the  $sp^3s^*$  tight-binding model is improved by increasing the number of neighboring interactions or the number of orbitals.

Jancu et al. [73, 74] included the d orbital into  $sp^3s^*$  tight-binding model with the combination of the nearest-neighboring interaction and spin-orbit coupling, called  $sp^3d^5s^*$  empirical tight-binding method. The additional d orbitals play the crucial role for the corrections of lowest conduction bands at X point. The band structures for many IV, III–V and nitride semiconductors such as C, Si, Ge, AlP, GaP, InP, AlAs, GaAs, InAs, AlSb, GaSb, InSb, GaN, AlN and InN are in an excellent agreement with pseudopotential method and experiments. Table 23.2 itemizes the references of the tight-binding parameterizations for the important semiconductors (mainly in IV, III–V and II–VI group).

## 23.4 Empirical Tight-Binding Theory of Core/Shell Nanocrystals

### 23.4.1 The $sp^3s^*$ Empirical Tight-Binding Description

For the demonstration of the studied nanostructures,  $sp^3s^*$  empirical tight-binding theory with the combination of the nearest neighboring interaction and spin-orbit coupling is utilized to investigate the core/shell semiconductor nanocrystals. The  $sp^3s^*$  empirical tight-binding method was initially introduced by Vogl [72] to obtain more accurate band structures than  $sp^3$  TB and consume the computationally requirement less than  $sp^3d^5s^*$  TB. The computational process starts with a definition of the atomic positions of the core/shell nanocrystals with the zinc-blende or wurtzite crystal structure depending on the available experiments. The single wave function is written as a linear combination of atomic orbitals localized on each atom given by:

$$|\psi\rangle = \sum_{R=1}^{N_{at}} \sum_{\alpha=1}^{10} C_{R,\alpha} |R, \alpha\rangle$$

where  $\alpha$  stands for the localized atomic orbitals on atom  $R$  with  $N_{at}$  being the total number of atoms inside the system. The index of  $\alpha$  from 1 to 5 stands for  $s \uparrow$ ,  $p_x \uparrow$ ,  $p_y \uparrow$ ,  $p_z \uparrow$  and  $s^* \uparrow$ , while the index of  $\alpha$  from 6 to 10 is defined as  $s \downarrow$ ,  $p_x \downarrow$ ,  $p_y \downarrow$ ,  $p_z \downarrow$  and  $s^* \downarrow$ . The coefficients  $C_{R,\alpha}$  determining the  $i$ th single-particle state and the corresponding single-particle energies are found by diagonalizing the empirical tight-binding Hamiltonian. The  $sp^3s^*$  empirical tight-binding Hamiltonian is given by:

$$\begin{aligned} H_{TB} = & \sum_{R=1}^{N_{at}} \sum_{\alpha=1}^{10} \varepsilon_{R\alpha} C_{R\alpha}^\dagger C_{R\alpha} + \sum_{R=1}^{N_{at}} \sum_{\alpha=1}^{10} \sum_{\alpha'=1}^{10} \lambda_{R\alpha\alpha'} C_{R\alpha}^\dagger C_{R\alpha'} \\ & + \sum_{R=1}^{N_{at}} \sum_{R'=1}^{N_{at}} \sum_{\alpha=1}^{10} \sum_{\alpha'=1}^{10} t_{R\alpha,R'\alpha'} C_{R\alpha}^\dagger C_{R'\alpha'} \end{aligned}$$

where the operator  $C_{R\alpha}^\dagger$  ( $C_{R\alpha}$ ) creates (annihilates) the particle on the orbital  $\alpha$  of atom  $R$ . The on-site orbital energies  $\varepsilon_{R\alpha}$ , spin-orbit coupling constant  $\lambda_{R\alpha\alpha'}$  and hopping matrix elements  $t_{R\alpha,R'\alpha'}$  connecting different orbitals situated on neighboring atoms are described in this Hamiltonian. For the heterostructure, the valence-band offset ( $E_v$ ) between core and shell is included in the tight-binding Hamiltonian. Therefore, all diagonal matrix elements of the core are shifted by  $E_v$  as compared to the shell diagonal matrix elements. The strain effect in the heterostructure is encompassed to provide a realistic description of the electronic states. The changes due to the strain are treated only by the scaling of inter-site matrix elements defined as:

$$t_{R\alpha, R'\alpha'} = t_{R\alpha, R'\alpha'}^0 \left( \frac{d_{R'_j R_j}^0}{d_{R'_j R_j}} \right)^{n_{kl}}$$

where  $t_{R\alpha, R'\alpha'}^0$  and  $t_{R\alpha, R'\alpha'}$  are the ideal and distorted hopping matrix elements, respectively.  $d_{R'_j R_j}^0$  and  $d_{R'_j R_j}$  are the bond lengths of unstrained and strained binary materials, respectively. From Harrison's  $d^{-2}$  rule [102],  $n_{kl} = 2.0$  is employed. Besides, the core/shell nanocrystals are passivated with the hydrogen atoms at the surface to avoid the formation of dangling bonds because these bonds may produce gap states and impede the calculations.

### 23.4.2 Oscillation Strength

To study the optical properties of the nanostructures, the oscillator strengths between the electron and hole states are demonstrated and analyzed. The oscillator strengths are calculated to determine optically allowed states of the dynamic polarization. The oscillation strengths  $f_{ij}$  between electron ( $i$ ) and hole ( $j$ ) states are defined as:

$$f_{ij} = \frac{2m_0}{\hbar^2} \left| \hat{e} \cdot \vec{D}_{ij} \right|^2 \times (E_i - E_j)$$

where  $m_0$  is the free-electron mass.  $E_i$  and  $E_j$  are the energies of electron ( $i$ ) and hole ( $j$ ) levels, respectively.  $\hat{e}$  are the polarized vectors (xy plane [110] and z axis [001]).  $\vec{D}_{ij}$  are the interacted dipole moments between transition states of electron ( $i$ ) and hole ( $j$ ) levels.

### 23.4.3 Optical Spectra

To understand the optical properties of nanostructure devices, the optical spectra are calculated with the combination of single-particle spectra obtained from empirical tight-binding model and Fermi's Golden rule. The formula of the optical intensity ( $I(E)$ ) is given by:

$$I(E) = \frac{2\pi}{\hbar} \sum_{n,m} \left| \langle \psi_{n,k=0}^v | E \vec{e} \cdot \vec{r} | \psi_{m,k=0}^c \rangle \right|^2 \delta(E_{n,k=0}^v - E_{m,k=0}^c - E)$$

Here,  $k = 0$  is the Gamma point in Brillouin zone. The indexes of  $m$  and  $n$  are symbolized for  $m$ th electron and  $n$ th hole levels.  $\psi_{m,k=0}^c$  and  $\psi_{n,k=0}^v$  are the electron

and hole wave functions, respectively.  $E_{m,k=0}^c$  and  $E_{n,k=0}^v$  are the electron and hole energies, correspondingly.  $\vec{e}$  are polarized vectors.

### 23.4.4 Radiative Lifetime

To understand the recombination between electron and hole, the calculations of radiative lifetime ( $\tau_{ij}$ ) between electron ( $i$ ) and hole ( $j$ ) states are determined. The equation is given by:

$$\tau_{ij} = \frac{3h^2 m_0 c^3}{8\pi^2 n e^2 (E_i^e - E_j^h)^2} f_{ij}$$

For the demonstration,  $m_0$  is the free-electron mass,  $n$  is the refractive index and  $f_{ij}$  are the oscillator strengths between electron ( $i$ ) and hole ( $j$ ) states.  $E_i^e$  and  $E_j^h$  are the single-particle energies of electron ( $i$ ) and hole ( $j$ ) states, respectively.

### 23.4.5 Many-Body Hamiltonian

Once the single-particle states  $\psi(r)$  and energies  $E_n$  are obtained by diagonalizing the empirical tight-binding Hamiltonian, the many-body Hamiltonian for the interacting electrons and holes is written in second quantization as: [103–105]

$$\begin{aligned} H_{many-body} = & \sum_i E_i^e c_i^\dagger c_i + \sum_i E_i^h h_i^\dagger h_i + \frac{1}{2} \sum_{ijkl} V_{ijkl}^{ee} c_i^\dagger c_j^\dagger c_k c_l \\ & + \frac{1}{2} \sum_{ijkl} V_{ijkl}^{hh} h_i^\dagger h_j^\dagger h_k h_l - \sum_{ijkl} V_{ijkl}^{eh,dir} c_i^\dagger h_j^\dagger h_k c_l + \sum_{ijkl} V_{ijkl}^{eh,exchg} c_i^\dagger h_j^\dagger c_k h_l \end{aligned}$$

Here, the operators  $c_i^\dagger$  ( $c_i$ ) and  $h_i^\dagger$  ( $h_i$ ) create (annihilate) the electron or hole in the state with energies  $E_i^e$  ( $E_i^h$ ). The two-body coulomb matrix elements are  $V_{ijkl}^{ee}$  for electron–electron interaction,  $V_{ijkl}^{hh}$  for hole–hole interaction,  $V_{ijkl}^{eh,dir}$  for electron–hole direct coulomb interaction and  $V_{ijkl}^{eh,exchg}$  for electron–hole exchange interaction. In the single excitonic case (contain one electron and one hole), the third and fourth term are therefore absent. Then, the single excitonic Hamiltonian is re-written as:

$$\begin{aligned} H_{single-exciton} = & \sum_i E_i^e c_i^\dagger c_i + \sum_i E_i^h h_i^\dagger h_i \\ & - \sum_{ijkl} V_{ijkl}^{eh,dir} c_i^\dagger h_j^\dagger h_k c_l + \sum_{ijkl} V_{ijkl}^{eh,exchg} c_i^\dagger h_j^\dagger c_k h_l \end{aligned}$$

The wave functions of the excitonic states are defined as the product of electron and hole wave functions:

$$\Phi_{ex} = \sum_{i,j} C_{i,j} \Psi_i^e(r_e) \Psi_j^h(r_h)$$

$\Psi_i^e$  and  $\Psi_j^h$  are the single-particle  $i$ th electron and  $j$ th hole wave functions, respectively. Finally, the energies and the coefficients  $C_{i,j}$  of the excitonic states can be obtained by diagonalizing the single excitonic Hamiltonian.

### 23.4.6 Examples of the Tight-Binding Calculations

Here, the examples in the implementation of the empirical tight-binding method with different orbital hybridizations on the different nanostructures are presented. In addition, the results corresponding to the electronic structures and optical properties of the examples are mainly presented in this chapter. Here, the example begins with the simple  $sp^3$  empirical tight-binding model. Niquet et al. [71] reported the electronic calculations of Si nanostructures using the  $sp^3$  empirical tight-binding model with third-nearest neighboring interactions and spin-orbit coupling. Using this parameterization, the band gap, Luttinger parameters and effective masses were properly fitted to experiment. The comparison of the confinement energies of Si nanocrystals was realized as a function of diameters. The empirical tight-binding data was compared against pseudopotential (PP) and local density approximations (LDA). The confinement energies of tight-binding model were not only in a good agreement with PP model in large sizes but also in an excellent agreement with LDA within the small clusters. Sukkabet [106, 107] reported the theoretical investigation of electronic structures and optical properties of InN and InSb nanocrystals via the  $sp^3s^*$  empirical tight-binding model with the nearest neighboring interactions and spin-orbit coupling. The structural and optical properties of InN and InSb nanocrystals are mainly dependent on their sizes, compositions and crystal structures. The example of the calculated band gaps in these nanocrystals was demonstrated. Figure 23.3 displayed the excitonic gaps of InSb nanocrystals as a function of the diameters. The optical band gaps of InSb nanocrystals were reduced with the increasing diameters due to the quantum confinement. The excitonic energies of tight-binding model were more consistent with the experimental data than those originally calculated by Efros and Rosen.

In case of the core/shell nanocrystals, there are several scientific works. This chapter mainly focuses on some important results of these nanostructures via  $sp^3s^*$  empirical tight-binding theory. Sukkabet [67] studied the electronic structures and optical properties of CdSe/ZnSe core/shell nanocrystals with experimentally synthesized sizes by  $sp^3s^*$  empirical tight-binding theory as a function of the growth shell thicknesses. The structural parameters of the CdSe/ZnSe core/shell nanocrystals were

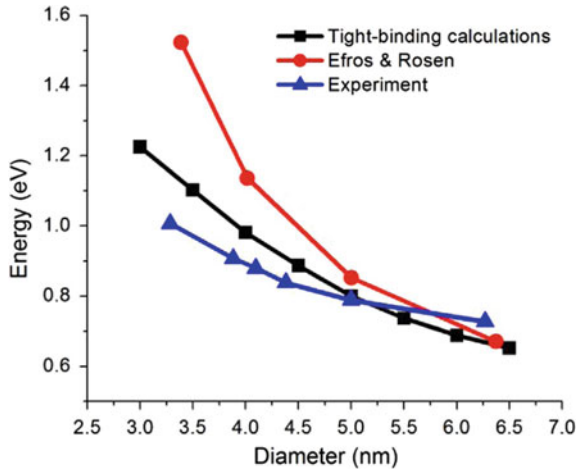


**Fig. 23.3** The excitonic gaps of InSb zinc-blende nanocrystals as a function of diameters [106]

employed from the experimental data of Reiss et al. [108]. The spherical shape of CdSe/ZnSe core/shell nanocrystals was consisted of CdSe core with diameter of 3.6 nm and ZnSe terminated shell thicknesses ( $t_s$ ) of 0.9, 1.8 and 2.7 monolayer (ML). For the demonstration of the electronic properties, the energies of electron and hole states under different shell thickness were displayed in Figs. 23.4 and 23.5, respectively. In the presence of the ZnSe shell, the electron and hole levels were improved in the comparison with those of single CdSe nanocrystals because of the

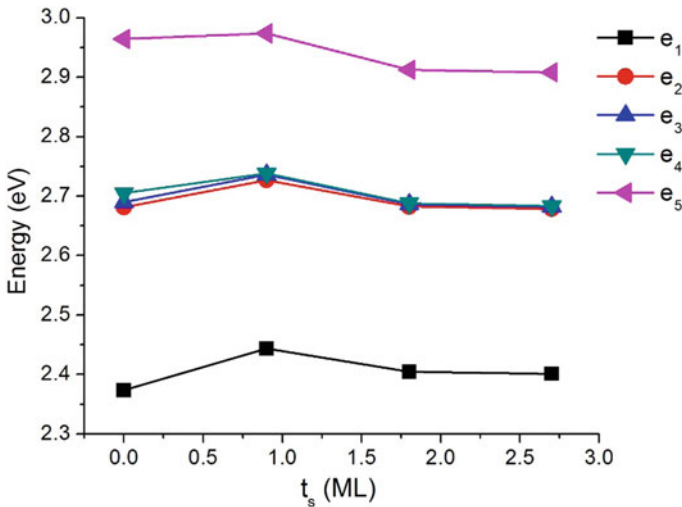


**Fig. 23.4** Electron energies as a function of ZnSe shell thicknesses (ML) [67]



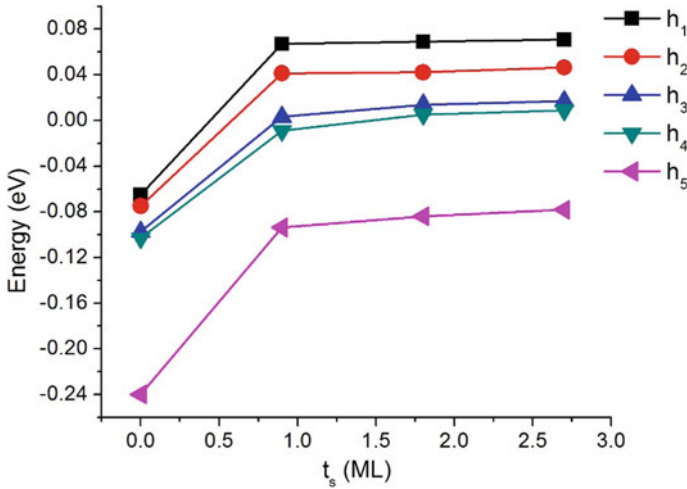


Fig. 23.5 Hole energies as a function of ZnSe shell thicknesses (ML) [67]

valence band offset between core and shell. Figure 23.6 illustrated the single-particle gaps, excitonic gaps and the size-tuneable absorption spectra of CdSe/ZnSe core/shell nanocrystals as a function of the ZnSe shell thicknesses. The single-particle gap was computed from the difference between the maximum hole and minimum electron state. The excitonic energies were achieved by diagonalizing the single excitonic Hamiltonian using the configuration interaction method. The results underlined that the reduction of the single-particle and excitonic gaps with increasing shell thickness reflected the quantum confinement. As the comparison, the  $sp^3s^*$  empirical

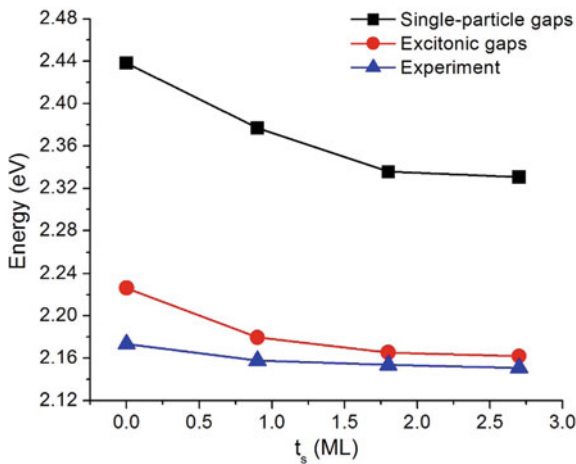
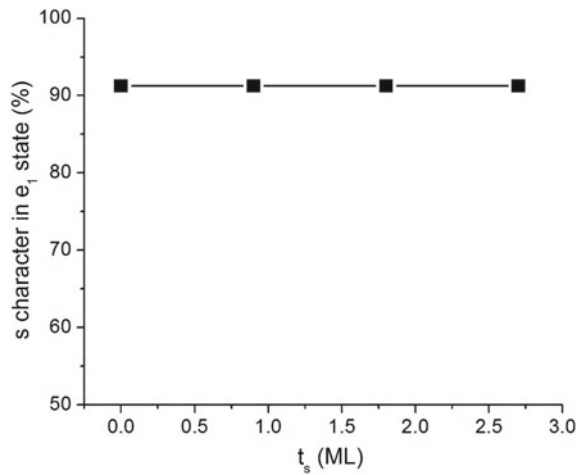


Fig. 23.6 The single-particle and excitonic gaps as a function of ZnSe shell thickness (ML) [67]

tight-binding calculations coincided well with optical band gaps from the experiment. In order to understand the behavior of orbital localized in the CdSe/ZnSe core/shell nanocrystals, the theoretical analysis of electron and hole character was also discussed. The ground electron states were characterized the s-like behavior in Fig. 23.7. In Figs. 23.8 and 23.9, the admixture of the p orbital contributed to the first-two hole states. In the presence of the ZnSe shell, the heavy-hole-like state in  $h_1$  and light-hole-like state in  $h_2$  were significantly improved in the comparison with the single CdSe nanocrystal. For the demonstration of the optical properties, the oscillator strength spectra ( $f_{ij}^{xy}$  and  $f_{ij}^z$ ) of dipole moments determined by the spatial symmetrical xy plane and z component were displayed in Figs. 23.10 and 23.11 as a function of the inter-band transition states between the electron ( $e_i$ ) and hole levels ( $h_j$ ) under

**Fig. 23.7** The s character in the ground electron state ( $e_1$ ) as a function of ZnSe shell thickness (ML) [67]



**Fig. 23.8** The heavy-hole character in the first hole state ( $h_1$ ) as a function of ZnSe shell thickness (ML) [67]

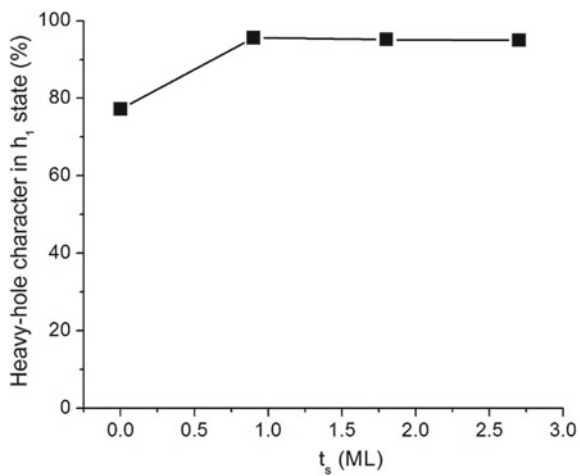


**Fig. 23.9** The light-hole character in the second hole state ( $h_2$ ) as a function of ZnSe shell thickness (ML) [67]

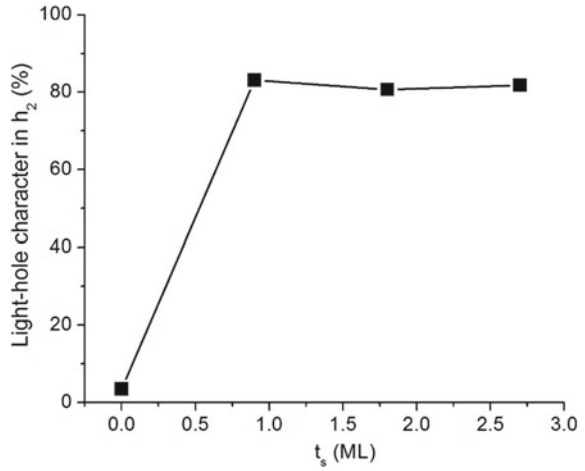


**Fig. 23.10** Oscillation strengths in xy plane ( $f_{ij}^{xy}$ ) as a function of ZnSe shell thickness (ML) [67]

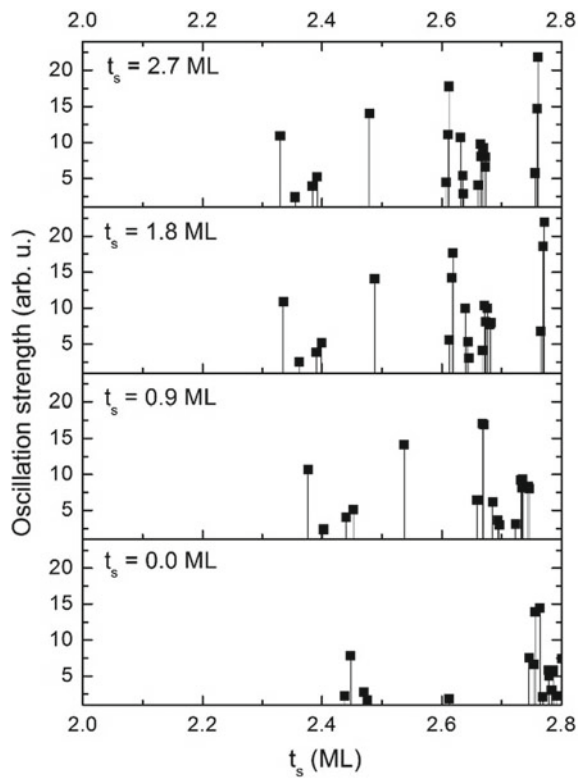
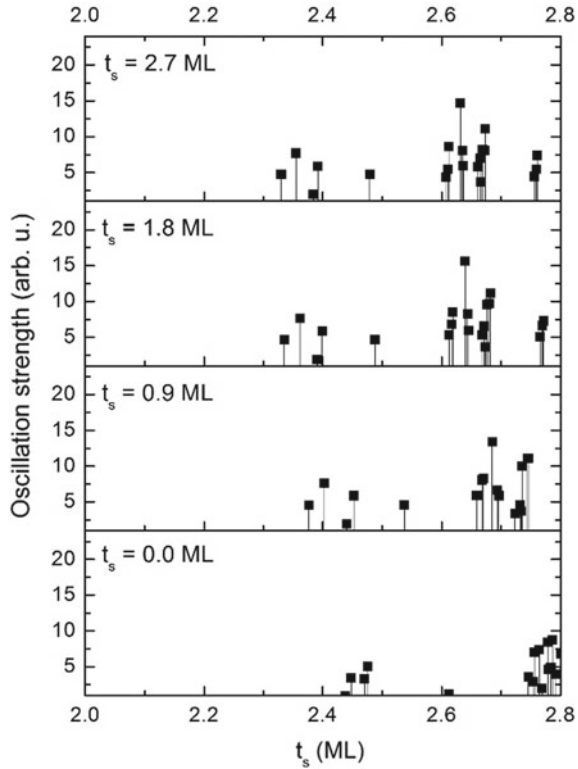


**Fig. 23.11** Oscillation strengths along z direction ( $f_{ij}^z$ ) as a function of ZnSe shell thickness (ML) [67]



various shell thicknesses, respectively. The oscillation strengths were sensitive with the shell thickness and polarized vectors (xy and z direction). The minor red shifts in the oscillation strength spectra were reported with the increasing shell sizes. The oscillation strengths were enhanced when passivating the ZnSe growth shell on CdSe core, showing the improved optical properties. To analyze the optical properties, the first-two inter-band transition was determined. By considering the first peak of the spectra contributed from  $e_1 - h_1$  transition, in the presence of the ZnSe shell the magnitudes of  $f_{ij}^{xy}$  were greater than those of  $f_{ij}^z$ . This was due to the fact that the dipole moment interactions between s-like ( $e_1$ ) and heavy-hole-like states ( $h_1$ ) along [109] plane were mainly more promoted than those along the [001] direction as described by the orbital characters in the previous Fig. 23.8. Therefore, the first peaks of the emission spectra were mostly donated by  $f_{ij}^{xy}$  terms. For the second peaks from  $e_1 - h_2$  transition, when coating ZnSe shell the magnitudes of  $f_{ij}^z$  were higher than those of  $f_{ij}^{xy}$  because the dipole moment interactions between s-like ( $e_1$ ) and light-hole-like states ( $h_2$ ) along the z direction were augmented. Hence, the majorities of the second peaks were from  $f_{ij}^z$ . As can be seen, the electronic structures and optical properties were mainly manipulated by the growth shell thickness with the implementation to novel optoelectronic applications.

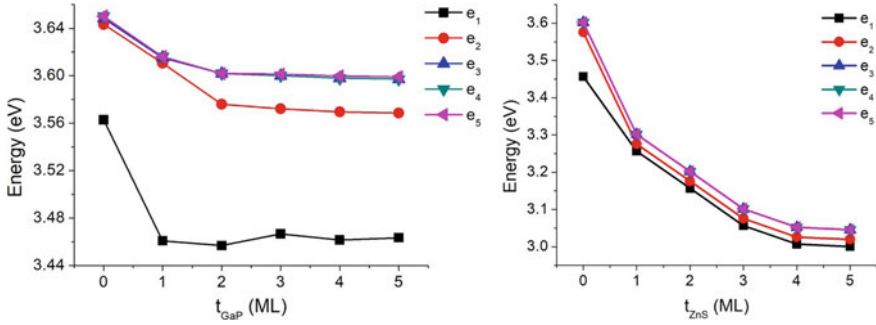


**Fig. 23.12** Electron energies of InP/GaP core/shell and InP/GaP/ZnS core/shell/shell nanocrystals as a function of internal shell ( $t_{GaP}$ ) and external shell ( $t_{ZnS}$ ) thicknesses, respectively [109]

In addition, the core/shell nanocrystals could be passivated by another growth shell of different material, called core/shell/shell nanocrystal. Thus, the electronic structures and optical properties were widely controlled within more structural parameters (external shell). Sukkabot [109] reported the improvement of the luminescence efficiency for InP nanocrystals by coating a GaP/ZnS multi shell in zinc-blende phase using the atomistic tight-binding theory and configuration interaction method. InP/GaP/ZnS core/shell/shell nanocrystals were considered to be a non-toxic material for customer applications. For the demonstration of the impact for the interior shell on the natural behaviors, InP core with diameter of 3.10 nm was passivated by layers of GaP internal shell ( $t_{GaP}$ ) from 0 to 5 monolayers (ML). To study the external shell dependence, thick layers of the ZnS external shell ( $t_{ZnS}$ ) from 0 to 5 ML were terminated on InP/GaP core/shell nanocrystal with InP core diameter of 3.10 nm and GaP internal shell thickness of 2 ML. Figure 23.12 demonstrated the electron energies of InP/GaP core/shell and InP/GaP/ZnS core/shell/shell nanocrystals as a function of the internal and external growth shell thicknesses. The electron energies were reduced with the increasing internal and external coated shell thicknesses. The hole energies of InP/GaP core/shell and InP/GaP/ZnS core/shell/shell nanocrystals were illustrated in Fig. 23.13 under different internal and external growth shell thicknesses. With the increasing growth shell thicknesses, the hole energies of InP/GaP core/shell and InP/GaP/ZnS core/shell/shell nanocrystals were improved. For the active applications in the optoelectronic devices, the optical band gaps of InP/GaP core/shell and InP/GaP/ZnS core/shell/shell nanocrystals as a functions of the internal and external growth shell thicknesses were presented in Fig. 23.14. The reduction of optical band gaps was obtained with the increasing internal and external growth shell thicknesses due to the quantum confinement effect. The optical band gaps changing across the visible wave lengths were carried out by varying the internal and external growth shell thicknesses. The optical properties of InP/GaP core/shell and InP/GaP/ZnS core/shell/shell nanocrystals were analyzed in the framework of ground-state oscillation strengths in Fig. 23.15. The oscillation strengths were improved when termi-

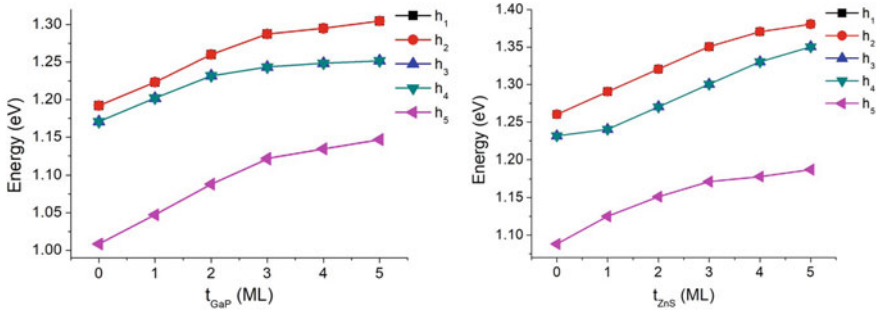


**Fig. 23.13** Hole energies of InP/GaP core/shell and InP/GaP/ZnS core/shell/shell nanocrystals as a function of internal shell ( $t_{GaP}$ ) and external shell ( $t_{ZnS}$ ) thicknesses, respectively [109]

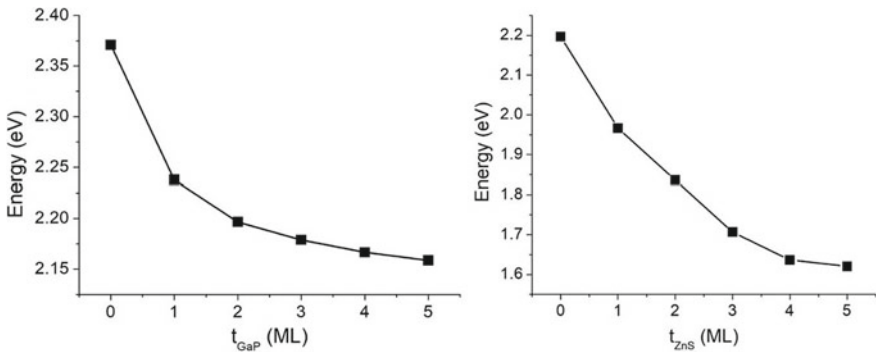


**Fig. 23.14** Optical band gaps of InP/GaP core/shell and InP/GaP/ZnS core/shell/shell nanocrystals as a function of internal shell ( $t_{GaP}$ ) and external shell ( $t_{ZnS}$ ) thicknesses, respectively [109]

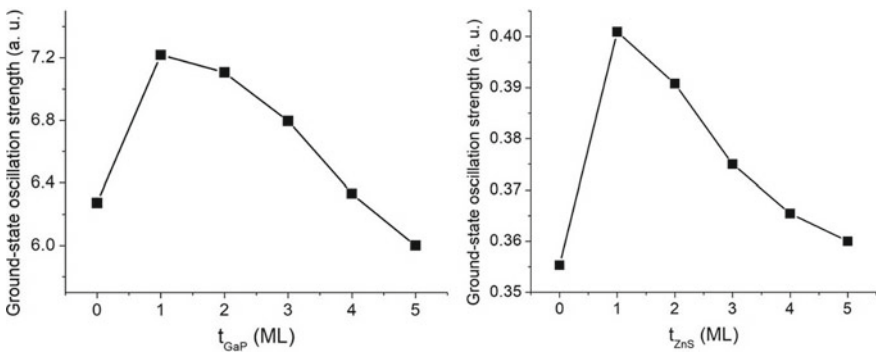


**Fig. 23.15** Oscillation strengths of InP/GaP core/shell and InP/GaP/ZnS core/shell/shell nanocrystals as a function of internal shell ( $t_{GaP}$ ) and external shell ( $t_{ZnS}$ ) thicknesses, respectively [109]

**Table 23.3** The references of theoretical studies for the important core/shell nanostructures (mainly in IV, III–V and II–VI group)

Systems	References		
	DFT	EPM	ETB
Si/Ge	[110, 111]		[112, 113]
InAs/InP			[114]
InAs/GaAs		[115]	[116, 117]
CdSe/CdS	[118, 119]	[66, 120]	[121, 122]
CdSe/ZnS	[123]		[124]
CdSe/ZnSe			[67]
CdTe/CdSe	[125]		[126]
ZnSe/ZnS	[127]		[128, 129]
ZnTe/ZnS			[130]
ZnTe/ZnSe			[131]

nating the internal and external shell, implying the enhancement of the optical properties. The oscillation strengths were progressively reduced as the internal and external shell thicknesses were increased. Passivation of GaP shell on InP core obviously improved the optical properties in the comparison with InP single nanocrystal. In addition, the optical properties in InP/GaP/ZnS core/shell/shell nanocrystals were enhanced when comparing to InP/GaP core/shell nanocrystals. By changing the sizes of the internal external coated shell, the guideline for designing the electronic structures and optical performance of these systems was finally achieved.

At the moment, there are several semiconductor core/shell nanocrystals, especially in IV, III–V and II–VI group. These systems have been widely determined by various experimental and theoretical methods. The theoretical description of semiconductor nanostructures is of essential prominence to examine fundamental physics before the actual manufacture. Table 23.3 itemizes the references of theoretical studies for the important core/shell nanostructures (mainly in IV, III–V and II–VI group). Here, theoretical investigations mainly focus on density functional theory (DFT), empirical pseudopotential method (EPM) and empirical tight-binding method (ETB).

## 23.5 Conclusion

Semiconductor core/shell nanocrystals are commonly applied in modern electronic and optoelectronic devices. Before actual fabrication, the theoretical description of semiconductor core/shell nanocrystals is of crucial importance. It is well known that atomistic approaches are essential to model the structural, electronic and optical properties of the approaching nanometric sizes. Here, the empirical tight-binding approach is successfully utilized because both of the computational efficiency and atomistic description are preserved. For the demonstration, the procedure of the

computations is structured as follow. The first step is to generate the atomic positions of core/shell nanocrystals with desired shape, core diameter and growth shell thickness. Due to the lattice mismatch induced by the difference in core and shell material, the valence force field method (VFF) is implemented to optimize the atomic positions. The total energy of this approach is described as the summation of the energies of the stretching and bending bonds with the integration of the fitting parameters which explain the behaviors of each binary. After minimizing the total energy by conjugate gradient method, the relaxed atomic positions and the strain distribution are achieved. Using the Schrodinger equation, the single-particle spectra are numerically obtained in the framework of atomistic tight-binding theory. Due to the optimized computational consume with the satisfied bulk band structure calculations,  $sp^3s^*$  empirical tight-binding theory with the combination of the nearest neighboring interaction and spin-orbit coupling is utilized to investigate the core/shell semiconductor nanocrystals. After obtaining the single particle states and energies by diagonalizing the empirical tight-binding Hamiltonian, the natural properties of the studied core/shell nanocrystals are carried out. Implementing the configuration interaction description, the many-body Hamiltonian is computationally solved via the exact diagonalization method in the combination of the single-particle spectra. Using the tight-binding model, the electronic structures and optical properties of several semiconductor core/shell nanocrystals are evaluated and present a good agreement with the other theoretical and experimental data. Therefore, the empirical tight-binding model is very promising for the simulation tool to support the project of nanostructure devices.

## References

1. M.J. Bowers, J.R. McBride, S.J. Rosenthal, J. AM. Chem. Soc. **127**, 15378 (2005)
2. P.O. Anikeeva, C.F. Madigan, S.A. Coe-Sullivan, J.S. Steckel, M.G. Bawendi, V. Bulovic, Chem. Phys. Lett. **424**, 120 (2006)
3. A.J. Nozik, Phys. E **14**, 115 (2002)
4. I. Gur, N.A. Fromer, M.L. Geier, A.P. Alivisatos, Science **310**, 462 (2005)
5. M.C. Hanna, A.J. Nozik, J. Appl. Phys. **100**, 074510 (2006)
6. P.V. Kamat, J. Phys. Chem. C **112**, 18737 (2008)
7. V.I. Klimov, A.A. Mikhailovsky, S. Xu, A. Malko, J.A. Hollingsworth, C.A. Leatherdale, H.J. Eisler, M.G. Bawendi, Science **290**, 314 (2000)
8. S. Achilefu, Technol. Cancer Res. Treat **3**, 393 (2004)
9. M. Bruchez, M. Moronne, P. Gin, S. Weiss, A.P. Alivisatos, Science **281**, 2013 (1998)
10. A. Mukherjee, S. Ghosh, J. Phys. D Appl. Phys. **45**, 195103 (2012)
11. M. Dahan, S. Levi, C. Luccardini et al., Science **302**, 442 (2003)
12. D. Loss, D.P. DiVincenzo, Phys. Rev. A **57**, 120 (1998)
13. C. Filgueiras, O. Rojas, M. Rojas, Annalen Der Physik, 2000207 (2020)
14. N.W. Hendrickx, W.L.L. Lawrie, L. Petit, A. Sammak, G. Scappucci, M. Veldhorst, Nat. Commun. **11**, 3478 (2020)
15. H. Qiao, Y.P. Kandel, K. Deng, S. Fallahi, G.C. Gardner, M.J. Manfra, E. Barnes, J.M. Nichol, Phys. Rev. X **10**, 031006 (2020)
16. B. Lassen, M. Willatzen, R. Melnik, L.C.L.Y. Voon, J. Mater. Res. **21**, 2927 (2006)



17. W. Kohn, J. Luttinger, *Phys. Rev.* **98**, 915 (1955)
18. J. Luttinger, *Phys. Rev.* **102**, 1030 (1956)
19. D.S. Citrin, Y.-C. Chang, *Phys. Rev. B* **40**, 5507 (1989)
20. J.-B. Xia, *Phys. Rev. B* **43**, 9856 (1991)
21. V.V.R. Kishore, B. Partoens, F.M. Peeters, *Phys. Rev. B* **86**, 165439 (2012)
22. V.R. Kishore, N. Čukarić, B. Partoens, M. Tadić, F. Peeters, *J. Phys. Condens. Matter* **24**, 135302 (2012)
23. B. Lassen, L. Lew Yan Voon, M. Willatzen, R. Melnik, *Solid State Comm.* **132**, 141 (2004)
24. P. Redliński, F. Peeters, *Phys. Rev. B* **77**, 075329 (2008)
25. V.R. Kishore, B. Partoens, F. Peeters, *Phys. Rev. B* **82**, 235425 (2010)
26. M. Persson, A. Di Carlo, *J. Appl. Phys.* **104**, 073718 (2008)
27. M. Persson, H.Q. Xu, *Nano Lett.* **4**, 2409 (2004)
28. M. Persson, H.Q. Xu, *Phys. Rev. B* **73**, 125346 (2006)
29. M. Persson, H.Q. Xu, *Phys. Rev. B* **73**, 035328 (2006)
30. Y. Niquet, *Nano Lett.* **7**, 1105 (2007)
31. Y. Niquet, *Phys. Rev. B* **74** (2006) 155304.
32. M. Luisier, A. Schenk, W. Fichtner, G. Klimeck, *Phys. Rev. B* **74**, 205323 (2006)
33. G. Liao, N. Luo, Z. Yang, K. Chen, H.Q. Xu, *J. Appl. Phys.* **118**, 094308 (2015)
34. G. Liao, N. Luo, K.-Q. Chen, H.Q. Xu, *J. Phys. Condens. Matter* **28**, 135303 (2016)
35. G. Liao, N. Luo, K.-Q. Chen, H.Q. Xu, *Sci. Rep.* **6**, 28240 (2016)
36. P.Y. Yu, M. Cordona, *Fundamentals of Semiconductors* (2001)
37. A. Di Carlo, *Semicond. Sci. Technol.* **18**, R1 (2003)
38. P. Harrison, *Quantum Wells, Wires and Dots*. Wiley (2006)
39. H. Haug, S.W. Koch, *Quantum Theory of the Optical and Electronic Properties of Semiconductors*. World Scientific (2005)
40. J.R. Chelikowsky, M.L. Cohen, *Phys. Rev. B* **14**(2), 556 (1976)
41. M.L. Cohen, V. Heine, *The Fitting of Pseudopotentials to Experimental Data and Their Subsequent Application*, volume 24 of *Solid State Physics*. Academic Press, New York (1970)
42. M.L. Cohen, T.K. Bergstresser, *Phys. Rev.* **141**(2), 789 (1966)
43. F. Ning, L.-M. Tang, Y. Zhang, K.-Q. Chen, *J. Appl. Phys.* **114**, 224304 (2013)
44. S. Cahangirov, S. Ciraci, *Phys. Rev. B* **79**, 165118 (2009)
45. A. Srivastava, N. Tyagi, R. Ahuja, *Solid State Sci.* **23**, 35 (2013)
46. C.L. Dos Santos, P. Piquini, *Phys. Rev. B* **81**, 075408 (2010)
47. S. Schulz, *Electronic and Optical Properties of Quantum Dots: A Tight-Binding Approach* (2007)
48. W. Trzeciakowski, *Phys. Rev. B* **38**, 12493 (1988)
49. M.G. Burt, *J. Phys. Condens. Matter* **4**, 6651 (1992)
50. C. Pryor, J. Kim, L.W. Wang, A.J. Williamson, A. Zunger, *J. Appl. Phys.* **83**, 2548 (1998)
51. V.G. Malyskin, I.P. Ipatova, V.A. Shchukin, *J. Appl. Phys.* **74**, 7198 (1993)
52. B. Jogai, *J. Appl. Phys.* **88**, 5050 (2000)
53. B. Jogai, *J. Appl. Phys.* **90**, 699 (2001)
54. O. Stier, *Electronic and Optical Properties of Quantum Dots and Wires* (2000)
55. R. Maranganti, P. Sharma, *A Handbook of Theoretical and Computational Nanotechnology*. American Scientific Publishers (2005)
56. T.S. Marshall, T.M. Wilson, *Phys. Rev. B* **50**, 15034 (1994)
57. H. Jiang, J. Singh, *Phys. Rev. B* **56**, 4696 (1997)
58. P.N. Keating, *Phys. Rev.* **145**, 637645 (1966)
59. R.B. Capaz, P. Kratzer, Q.K.K. Liu, R. Santoprete, B. Koiller, M. Scheffler, *Phys. Rev. B* **68**, 235311 (2003)
60. J.H. Seok, J.Y. Kim, *Appl. Phys. Lett.* **78**, 3124 (2001)
61. L.-W. Kim, A. Zunger, *Phys. Rev. B* **57**, R9408 (1997)
62. D.S. Yadav, C. Kumar, *Int. J. Phys. Sci.* **8**, 1174 (2013)
63. W.W. Hager, H. Zhang, *SIAM J. Optim.* **16**, 170 (2005)
64. W.W. Hager, H. Zhang, *ACM Trans. Math. Softw.* **32**, 113 (2006)

65. W.W. Hager, H. Zhang, *Pac. J. Optim.* **2**, 35 (2006)
66. Y. Luo, L.-W. Wang, *ACS Nano* **4**, 91 (2010)
67. W. Sukkabot, *Comput. Mater. Sci.* **96**, 336 (2015)
68. J.C. Slater, G.F. Koster, *Phys. Rev.* **94**, 1498 (1954)
69. D.J. Chadi, *Phys. Rev. B* **16**, 790 (1977)
70. D.J. Chadi, M.L. Cohen, *Phys. Stat. Sol. (b)* **68**, 405 (1975)
71. Y.M. Niquet et al., *Phys. Rev. B* **62**, 5109 (2000)
72. P. Vogl, H.P. Hjalmarson, J.D. Dow, *J. Phys. Chem. Solids* **44**, 365 (1983)
73. J.-M. Jancu, R. Scholz, F. Beltram, F. Bassani, *Phys. Rev. B* **57**, 6493 (1998)
74. J.-M. Jancu, F. Bassani, F. Della Sala, R. Scholz, *Appl. Phys. Lett.* **81**(25), 4838 (2003)
75. G. Klimeck, R.C. Bowen, T.B. Boykin, C. Salazar-Lazaro, T.A. Cwik, A. Stoica, *Superlattices Microstruct.* **27**, 77 (2000)
76. C. Tserbak, H.M. Polatoglou, G. Theodorou, *Phys. Rev. B* **47**, 7104 (1993)
77. Q.M. Ma, K.L. Wang, J.N. Schulman, *Phys. Rev. B* **47**, 1936 (1993)
78. G. Grosso, C. Piermarocchi, *Phys. Rev. B* **51**, 16772 (1995)
79. D.N. Talwar, Z.C. Feng, *Phys. Rev. B* **44**, 3191 (1991)
80. J.N. Schulman, Y.-C. Chang, *Phys. Rev. B* **31**, 2056 (1985)
81. T.B. Boykin, J.P.A. van der Wagt, J.S.Jr. Harris, *Phys. Rev. B* **43**, 4777 (1991)
82. A. Di Carlo, P. Lugli, *Semicond. Sci. Technol.* **10**, 1673 (1995)
83. A. Di Carlo, A. Reale, L. Tocca, P. Lugli, *IEEE J. Quantum Electron.* **34**, 1730 (1998)
84. H. Dierks, G.Z. Czycholl, *Phys. Rev. B* **99**, 207 (1996)
85. K. Shim, H. Rabitz, *Phys. Rev. B* **57**, 12874 (1998)
86. T.B. Boykin, *Phys. Rev. B* **51**, 4289 (1995)
87. G. Theodorou, G. Tsegas, *Phys. Rev. B* **61**, 10782 (2000)
88. D. Olguin, R. Baquero, R. de Coss, *Rev. Mex. Fis.* **47**(1), 43 (2001)
89. D. Bertho, D. Boiron, A. Simon, C. Jouanin, C. Proester, *Phys. Rev. B* **44**, 6118 (1991)
90. Z.Q. Li, Q. Pötz, *Phys. Rev. B* **46**, 2109 (1992)
91. D. Bertho, J.M. Jancu, C. Jouanin, *Phys. Rev. B* **48**, 2452 (1993)
92. E.G. Wang, C.-F. Chen, C.S. Ting, *J. Appl. Phys.* **78**, 1832 (1995)
93. A. Kobayashi, O.F. Sankey, S.M. Volz, J.D. Down, *Phys. Rev. B* **28**, 935 (1983)
94. P.E. Lippens, M. Lannoo, *Phys. Rev. B* **41**, 6079 (1990)
95. J. Perez-Conde, A.K. Bhattacharjee, *Phys. Rev. B* **63**, 245318 (2001)
96. M. Fornari, H. H. Chen, L. Fu, R. D. Graft, D. J. Lohrmann, S. Moroni, G. Pastori Parravicini, L. Resca, M.A. Stroschio, *Phys. Rev. B* **55**, 16339 (1997)
97. J. Perez-Conde, A.K. Bhattacharjee, M. Chamarro, P. Lavallard, V.D. Petrikov, A.A. Lipovskii, *Phys. Rev. B* **64**, 113303 (2001)
98. A. Kobayashi, O.F. Sankey, J.D. Down, *Phys. Rev. B* **25**, 6367 (1983)
99. K.C. Hass, H. Eherenreich, B. Velicky, *Phys. Rev. B* **27**, 1088 (1983)
100. M. Dib, M. Chamarro, V. Voliotis, J.L. Fave, C. Guenard, P. Roussignol, T. Gacoin, J.P. Boilot, C. Delerue, G. Allan, M. Lannoo, *Phys. Status Solidi B* **212**, 293 (1999)
101. J.P. LaFemina, C.B. Duke, *J. Vac. Sci. Technol. A* **9**, 1847 (1991)
102. W.A. Harrison, *Elementary Electronic Structure*. World Scientific Publishing Company (1999)
103. M. Zielinski, M. Korkusinski, P. Hawrylak, *Phys. Rev. B* **81**, 085301 (2010)
104. M. Korkusinski, M.E. Reimer, R.L. Williams, and P. Hawrylak, *Phys. Rev. B* **79**, 035309 (2009)
105. K. Leung, K.B. Whaley, *Phys. Rev. B* **56**, 7455 (1997)
106. W. Sukkabot, *Mater. Sci. Semicond. Process.* **27**, 51 (2014)
107. W. Sukkabot, *Mater. Sci. Semicond. Process.* **38**, 142 (2015)
108. P. Reiss, J. Bleuse, A. Pron, *Nano Lett.* **2**(7), 781 (2002)
109. W. Sukkabot, *Comput. Mater. Sci.* **161**, 46 (2019)
110. N. Scott Bobbitt, J.R. Chelikowsky, *J. Chem. Phys.* **144**(12), 124110 (2016)
111. E.L. de Oliveira, E.L. Albuquerque, J.S. de Sousa, G.A. Farias, F.M. Peeters, *J. Phys. Chem. C* **116**, 7 (2012)
112. M.O. Nestoklon, A.N. Poddubny, P. Voisin, K. Dohnalova, *J. Phys. Chem. C* **120**, 33 (2016)

113. I.D. Avdeev, A.V. Belolipetsky, N.N. Ha, M.O. Nestoklon, I.N. Yassievich, *J. Appl. Phys.* **127**, 114301 (2020)
114. W. Sukkabot, *Phys. E Low-Dimens. Syst. Nanostruct.* **63**, 235 (2014)
115. H.Y.S. Al-Zahrani, J. Pal, M.A. Migliorato, G. Tse, D. Yu, *Nano Energy* **14**, 382 (2015)
116. Y.M. Niquet, *Phys. Rev. B* **74**, 155304 (2006)
117. Y.M. Niquet, *Nano Lett.* **7**(4), 1105 (2007)
118. V. Kocevski, J. Ruzs, O. Eriksson, D.D. Sarma, *Sci. Rep.* **5**, 10865 (2015)
119. L. Zhu, et al., *IOP Conf. Ser. Mater. Sci. Eng.* **490**, 022021 (2019)
120. H. Eshet, M. Grünwald, E. Rabani, *Nano Lett.* **13**(12), 5880 (2013)
121. W. Sukkabot, *Mater. Sci. Semicond. Process.* **34**, 14 (2015)
122. A. Jain, O. Voznyy, S. Hoogland, M. Korkusinski, P. Hawrylak, E.H. Sargent, *Nano Lett.* **16**(10), 6491 (2016)
123. X. Zhai, R. Zhang, J. Lin, Y. Gong, Y. Tian, W. Yang, X. Zhang, *Cryst. Growth Des.* **15**(3), 1344 (2015)
124. W. Sukkabot, *Mater. Sci. Semicond. Process.* **27**, 1020 (2014)
125. L. Zhang, Z. Lin, J.-W. Luo, A. Franceschetti, *ACS Nano* **6**(9), 8325 (2012)
126. W. Sukkabot, *Comput. Mater. Sci.* **111**, 23 (2106)
127. S.C. Pandey, J. Wang, T.J. Mountziaris, D. Maroudasa, *J. Appl. Phys.* **111**, 113526 (2012)
128. W. Sukkabot, *Superlattices Microstruct.* **75**, 739 (2014)
129. W. Sukkabot, *Mater. Sci. Semicond. Process.* **41**, 252 (2016)
130. W. Sukkabot, *Comput. Mater. Sci.* **101**, 275 (2015)
131. W. Sukkabot, *Physica E* **74**, 457 (2015)